Araştırma Makalesi / Research Article

Enhancement of Optical and Photonic Properties of the Micro-sized ZnO Particles by Cerium Doping

Ramazan DALMIŞ[1,*]

[1] *Dokuz Eylul University, Department of Metallurgical and Materials Engineering, Buca, 35390, Izmir, Turkey.*

Corresponding author e-mail: ramazan.dalmis@deu.edu.tr ORCID ID: http://orcid.org/0000-0002-5508-2539

Keywords
ZnO micro-particle; Ce dopant;
Photoluminescence;
Photocatalytic;
Characterization

Abstract

Water shortage is one of the most urgent issues today, owing to rising population and environmental reasons. The most significant thing that humanity can do to solve this situation is to recycle waste or contaminated water. ZnO has been widely employed for photocatalytic applications due to its unique features. It was aimed to improve the photocatalytic properties of the micron-sized ZnO particles by doping with Cerium dopant, which is a rare earth element and used in many photocatalytic studies. Structural, morphological, optical, and photocatalytic properties were characterized to examine the effect of the Ce dopant ratio. The increased grain size demonstrated that Ce^{4+} was efficiently integrated into the ZnO lattice. Ce doping into the Wurtzite ZnO lattice improved both the emission and photocatalytic efficiency of the micro-sized ZnO particles. Additionally, it was revealed that the Ce doping procedure is more effective than grain size on the photocatalytic efficiency.

Mikro Boyutlu ZnO Parçacıklarının Optik ve Fotonik Özelliklerinin Seryum Katkılama ile İyileştirilmesi

Anahtar kelimeler
ZnO mikro-parçacık; Ce katkılama;
Fotolüminesans;
Fotokatalitik;
Karakterizasyon

Öz

Artan nüfus ve çevresel nedenlerle su kıtlığı günümüzün en acil sorunlarından biridir. Bu durumu çözmek için insanlığın yapabileceği en önemli şey kirli suları geri dönüştürmektir. ZnO, benzersiz özellikleri nedeniyle fotokatalitik proses uygulamaları için yaygın olarak kullanılmaktadır. Sol-jel yöntemiyle üretilen mikron boyutlu ZnO partiküllerinin, nadir toprak elementi olan Seryum katkı maddesi katkılanarak fotokatalitik özelliklerinin iyileştirilmesi amaçlanmıştır. Ce katkı oranının etkisini incelemek için yapısal, morfolojik, optik ve fotokatalitik özellikler karakterize edildi. Artan tane boyutu, Ce^{4+}'nın ZnO kafesine verimli bir şekilde entegre olduğunu gösterdi. Wurtzite ZnO kafesine Ce katkısı, mikro boyutlu ZnO parçacıklarının hem emisyonunu hem de fotokatalitik verimliliğini iyileştirdi. Ayrıca fotokatalitik verim üzerinde Ce doping işleminin tane boyutundan daha etkili olduğu ortaya çıkmıştır.

1. Introduction

Environmental contamination has become a severe hazard to humanity as industry and civilization have grown rapidly (A. Gupta, Saurav and Bhattacharya 2015). Water pollution caused by the discharge of several contaminants from the industry has worsened the water quality. Therefore, its management is a major problem (L. Li *et al*. 2015). As natural purification cannot remove such harmful organic contaminants from water sources, various attempts have been carried out to identify adequate procedures for their total removal (Choudhary, Bisht, Satpati and Mohapatra 2021). The photodecomposition of these contaminants has evolved as an important option in recent decades and has been widely employed (Yang *et al*. 2016). Because of their variable band gap, cheap production cost, and favorable optical features, semiconductor-assisted photocatalysis has attracted interest (Xu, Anusuyadevi, Aymonier, Luque and Marre 2019).

Various semiconductor materials, such as ZnO, TiO$_2$, Fe$_2$O$_3$, CeO$_2$, SnO$_2$, and WO$_3$, have been employed for photocatalytic degradation in water and wastewater treatment to eliminate environmental pollutants (Demirci, Dikici, Tuncay ve Kaya 2020, Singh and Borthakur 2018). Among these semiconductor materials, ZnO has been preferred for photocatalytic applications due to its flexible, nontoxic, low cost, and distinctive electrical and optical features (Bomila, Suresh and Srinivasan 2019). Also, ZnO-based materials are widely used in various applications, including solar cells, chemical- and bio-sensors, ultraviolet (UV) lasers, light-emitting diodes (LEDs), photo-detectors, piezoelectric transducers, and actuators, hydrogen storage, photocatalysts, and soon, batteries (Kumar *et al*. 2015, Thambidurai, Muthukumarasamy, Velauthapillai and Lee 2014).

To a certain extent, doping ZnO nanoparticles increases surface flaws, which may shift absorption toward the visible area. Some studies have been conducted in order to dope rare earth metals (Er, Yb, La, Nd, and Ce) into the interstitial locations of ZnO crystals (H. L. Li, Lv, Li and Yu 2014, Sinha, Ray, Bhandari, Godara and Kumar 2014, Zamiri, Lemos, Reblo, Ahangar and Ferreira 2014). Rare earth metal-doped semiconductor nanomaterials have found widespread use in lasers, amplifiers, thin film electroluminescent devices, and optoelectronic/cathodoluminescent devices (Sinha *et al*. 2014, Zamiri *et al*. 2014). Rare earth ion doping can build traps for photo-generated charge carriers, by lowering the rate of electron–hole pair recombination (Sin, Lam, Lee and Mohamed 2014). Thus, hydrothermal, spraypyrolysis, radio frequency sputtering, sol–gel, chemical spray, thermal evaporation, and other techniques have been used to create lanthanide-doped ZnO (Kumar *et al*. 2015).

Studies on the photocatalytic properties of the Ce-doped ZnO materials have already been conducted. However, these studies have generally focused on Ce doping to the nano-sized structures (particles, rods, pindles etc.) (Choudhary *et al*. 2021, Karidas, Veena, Pujari, Krishna and Chunduru 2020, Kumar *et al*. 2015, Pathak, Coetsee-Hugo, Swart, Swart and Kroon 2020). For example, Kumar *et al*. investigated Ce doped ZnO nanoparticles for the photocatalytic degradation of direct red-23 dye (Kumar *et al*. 2015). They discovered that Ce-doped ZnO nanoparticles had significant photocatalytic activity, and that the degradation percentage increased with increasing Ce concentration (Kumar *et al*. 2015).

Nanotechnology may significantly improve many features of daily life for people, such as by enabling the production of clean energy and pure drinking water (Djaja and R. 2013). However, there is little information available regarding the exposure to nanoparticles or their effects on human health and safety in working environments, making it impossible to make an accurate risk assessment (Savolainen *et al.* 2010. Particularly, the separation of the photocatalytic particles to be used from water is of critical importance. Therefore, the development of micro-sized photocatalysts with high photocatalytic efficiency will be an important advantage. However, studies on Ce doping of micron-sized ZnO particles and its effect on their optical and photocatalytic properties are scarce. Therefore, this study characterizes the structural, morphological, optical, and photocatalytic properties of the 0.5%-2% Ce doped micro-particles, revealing the effect of the doping process. XRD, XPS, Powder Size Distribution, SEM, Photoluminescence spectrofluorometer, and photocatalytic tests analyzed the properties of the particles produced using the sol-gel method.

2. Experimental Procedure

2.1 Sol- Gel Production

To produce ZnO particles, zinc nitrate hexahydrate (Zn(NO$_3$)$_2$6H$_2$O, 99%, Aldrich Chemistry) was used as the initial raw material. In 300 ml absolute ethanol, 59.488 g of zinc nitrate hexahydrate was added. To create a homogeneous and clear solution, the solution was mixed for 30 minutes to finish the hydrolysis process. Cerium nitrate hexahydrate was added to the precursor solution in various concentrations (0, 0.5, 1, and 2 mole percent) with steady stirring until full dispersion. Following the creation of the transparent sol, 3 mL of glacial acetic acid and 0.1 mole of trietanolamin were added to the solution, as the chelating agent. Later, vigorously

stirred for 24 hours to enhance the gel formation. The powders were then annealed for 2 hours at 500°C. Thus, doped and undoped ZnO particles were obtained.

2.2 Characterization Methods

The crystal structures of the particles were determined using a Rigaku ULTIMA 3-Rint 2200/PC system X-ray diffractometer (XRD) in the 2θ range of 3–90, using Cu Kα with a wavelength of 0.1542 nm radiation produced with 40 kV and 36 mA current settings. The XPS measurements of the particles were carried out by a Thermo-Scientific Instrument equipped with an Al-Kα irradiation source (1486.7 eV). The XPS survey scans were performed from -10 eV to 1350 eV with a scanning speed of 1 eV, by applying a pass energy of 150 eV. Each sample was scanned 20 times from a single point. Calibration of the instrument was performed according to the gold $4f_{7/2}$.

The Malvern Nano ZS device, using the dynamic light scattering method, measured powder size distribution (PSD). The particle morphologies of the samples were studied using Zeiss Sigma 500 field emission scanning electron microscope. Steady-state excitation/emission spectra of the particles were recorded by an FLS920 spectrofluorometer from Edinburgh Instruments. The degradation of methylene blue (MB) in an aqueous solution under UV light was used to investigate the photocatalytic activity of the ZnO particles. To achieve an adsorption–desorption equilibrium of MB on the surface of the particles, 0.15 g particle were suspended in 50 ml of 10^{-5} M MB aqueous solution, which was magnetically agitated for 60 minutes in the dark medium.

3. Results and Discussions

3.1 XRD Analysis

The intensity data of the calcinated ZnO-based powder samples were gathered throughout a 20-90° range. The general XRD patterns of the ZnO powders are presented in Figure 1 (a). As can be observed from Fig. 1(a) diffraction peaks were located at the angles (2θ) of 31.86°, 34.54°, 36.36°, 47.66°, 56.68°, 62.94°, 66.44°, 68.02°, 69.16°, 72.68°, corresponding to the crystalline planes of the hexagonal Wurtzite zinc oxide structure (100), (002), (101), (102), (110), (103), (112), (201), (004) and (202), respectively (Al Abdullah, Awad, Zaraket, & Salame, 2017). All of the diffraction peaks matched the JCPDS number of 00-036-1451, and there were no secondary peaks other than ZnO. The peak at 2θ = 36.29° with (101) miller index plane exhibited the highest intensity, which is the major peak for the samples (see Fig. 1 (a)).
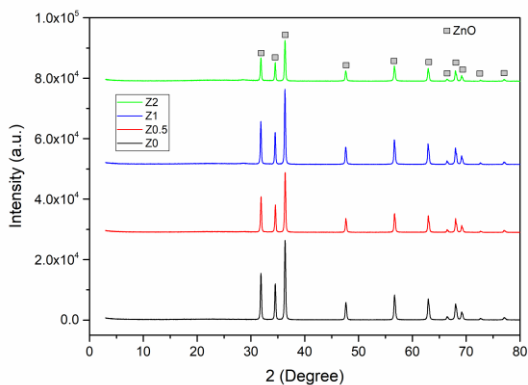
To show the Ce dopant effect, diffraction peaks at the (101) plane are presented in Fig. 1 (b). As can be observed from Fig. 1 (b), there is a considerable shift at the (101) peak after the doping process. The peak, belonging to the undoped sample was 36.36°, shifted to 36.34° after doping by the maximum Ce dopant. However, no linear change was observed between the dopant ratio and the peak shift level. For example, after 1% Ce doping, it caused a shift from 36.36° to 36.32°, causing more shifts than the maximum doping (2% Ce). Additionally, the peak intensity value was also seen to decrease, in proportion to the amount of dopant, by almost half after the doping process. The Debyee-Scherrer equation was used to compute the average crystalline sizes of the samples, using FWHM values of the (101) peak.

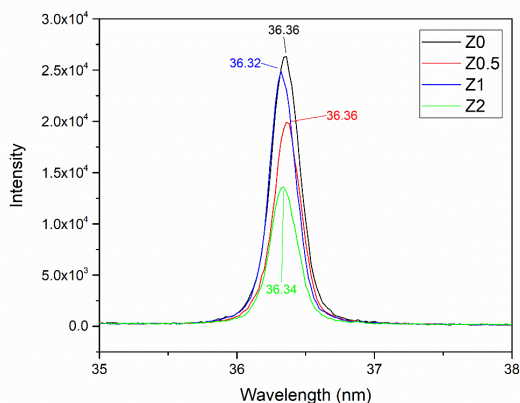$$D = (0.89 \times \lambda) \times (\beta \times cos\theta) \qquad (1)$$

where D is crystalline size, λ is the wavelength of radiation, β is full of half maximum of 2θ (101) peak, θ is the angle of the (101) XRD peak (Keskin, Dalmis, Birlik ve Azem 2020). Calculated average crystallite sizes of the samples with 2θ and full width half-maximum (FWHM) values are presented in Table 1.

The grain size, which was 34.02 nm before doping, increased to 36.92 nm with 1% Ce addition and became 35.67 nm with 2% Ce addition. That is, the addition of a Ce atom to the ZnO crystal structure increases grain size. Ce^{4+} and Ce^{3+} are the two distinct oxidation states of the Ce, yet the Ce^{4+} oxidation state is far more stable in the presence of air than the Ce^{3+} oxidation state (Subramanian *et al*. 2010). Since the ionic radii of the Zn^{2+} (7.4 Å) and O^{2-} (12.6 Å) ions in the ZnO content are different from Ce^{4+} (9.2 Å)

ionic radii, it causes distortions in the lattice structure (Anandan and Miyauchi 2011).

(a)

(b)

Figure 1. (a) General XRD patterns of the ZnO powders and (b) detailed pattern of the (101) diffraction peak according to the amount of Ce dopant ratio.

Table 1. Average crystalline sizes of the samples with related peak information

Sample Name	2θ	FWHM (Deg.)	Crystallite size (nm)
Z0	36.36	0.2567	34.02
Z0.5	36.36	0.2472	35.33
Z1	36.32	0.2366	36.92
Z2	36.34	0.2449	35.67

The absence of a new peak indicating the formation of a phase in XRD indicates that the Ce atom is located in substitutional or in one of the interstitial positions (Sharma, Sharma, Kumar and Sharma

2016). Compared to the undoped Z0 sample, all the doped samples have a larger crystallite size. The improvement in crystallite size shows that Ce^{4+} has been effectively absorbed into the ZnO lattice, where it replaces Zn^{2+} ion. Given that the doping ions are positioned in the tetrahedral sites via Zn^{2+} ion substitution, the electrical neutrality of the ZnO crystal necessitates the formation of $Ce_{Zn}^{\cdot\cdot}$ (Ce ion with two positive charge at the Zn position according to the Kröger-Vink notation) structure (Anandan & Miyauchi, 2011). However, the crystallite size, which increased up to a 1% Ce addition rate, showed a decrease with 2% Ce addition. This decrease in crystallite size might be attributed to the interstitial incorporation of Ce ions ($Ce_i^{\cdot\cdot\cdot}$) in ZnO matrix with increasing Ce concentration (Djaja and R. 2013). Thus, the nucleation process of ZnO and/or Ce atoms forms segregation at grain boundaries (Chelouche *et al.* 2017). As the Ce ratio rises, so does the number of nucleation sites, which may put a drag force on the motion of the crystallite border and hinder crystallite expansion (Chelouche *et al.* 2017).

3.2. XPS Analysis
The XPS analysis was performed to examine and get chemical information and the oxidation states of the components in ZnO particles. Fig. 2 (a) displays the XPS survey spectra of ZnO-based samples with various Ce dopant concentrations. It can be concluded that all samples consist of Zn, O, and C elements. Ce can be observed in all doped samples. The main peaks for Zn and O were clearly visible (see Fig. 2).
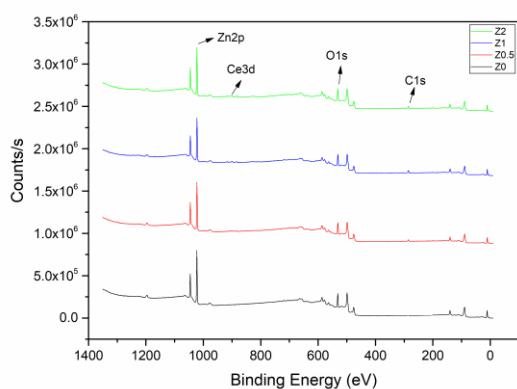
Carbon exists on all sample surfaces (Fig. 2) because it has been absorbed from the environment and cannot be eliminated from the surface (Demirci *et al*. 2020). The elemental composition results obtained from the XPS analysis are given in Table 2. It is observed that Zn and O, which have the highest element ratios, are between 36.92%-32.83% and 42.03%-39.43% values, respectively. The very high carbon ratio of about 25% may be due to the sol-gel process. During the removal of organic structures from the body by the calcination process, excess carbon may be left. Mole ratios of the Ce dopant were determined in the range of 0.91% to 1.50% in

the doped samples. As shown in Table 2, the determined Ce ratio is close to the theoretical dopant ratios. It is consistent that the Ce by mole ratio increases as the theoretical Ce ratio increases.
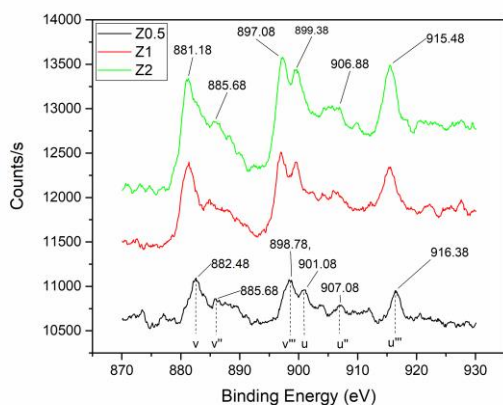
The binding maxima at 1022.38 and 1045.48 eV (Fig. 2 (a)) are possibly attributed to the Zn-O bond, which corresponds to Zn^{2+} in the ZnO structure (Reddy *et al*. 2019). Samples exhibit a characteristic O 1s peak at 531.18 eV, which can be attributed to OH bonds and, as a result, the presence of the O^{2-} ion on the ZnO surface (Demirci *et al*. 2020).

Table 2. Elemental composition results according to the XPS analysis

Samples	Chemical Contents (%mole)			
	Zn2p	O1s	Ce3d	C1s
Z0	36.92	42.03	-	21.05
Z0.5	38.04	41.53	0.91	19.52
Z1	32.83	39.43	1.32	26.42
Z2	32.88	40.52	1.50	25.10

High-resolution XPS scans on Ce 3d peaks for Z0.5-Z2 samples are presented in Fig. 2 (b). The Ce 3d spectrum of the ZnO:Ce samples consists of six peaks (two multiplets) specifically u ($3d_{3/2}4f^2O_{2p4}$), v ($3d_{5/2}4f^2O_{2p4}$), u^{11} ($3d_{3/2}4f^1O_{2p5}$), v^{11} ($3d_{5/2}4f^1O_{2p5}$), u^{111} ($3d_{3/2}4f^0O_{2p6}$), and v^{111} ($3d_{5/2}4f^0O_{2p6}$) as shown in Fig. 3 (b). These two multiplets are allocated to the spin-orbit split $3_{d5/2}$ and $3_{d3/2}$ core holes. The presence of tetravalent Ce^{4+} in particles is distinguished by spin orbital multiplets (v,u) and a peak at a higher binding energy of 916 eV. All six binding energy peaks in the presence of tetravalent Ce^{4+} ions according to the XPS examination of the Ce 3d spectrum (Anandan and Miyauchi 2011).

3.3 Powder Size Distribution

Powder size distribution (PSD) charts of the samples are presented in Fig. 3. Generally, the first thing about the graph draws attention is that the particle distributions of all samples exhibit a wide spectrum. Looking at the charts (see Fig. 3), it is seen that Z0 and Z2 have similar distributions, yet Z2 shows lower grain size distribution compared to Z0. It can be observed that the highest particle size belongs to the Z0 sample. The Z0.5 sample stands out as having the lowest particle size. Sample Z1 exhibits a higher (than Z0.5) and narrower (than others) particle size distribution. Considering the values calculated using the particle size analyses, Z0, Z0.5, Z1, and Z2 samples have average particle size values of **581.0** nm, **410.8** nm, **563.6** nm and **508.3** nm, respectively.

(a)

(b)

Figure 2. XPS survey spectra of (a) ZnO powders with various concentrations of Ce ions, and (b) focused high resolution XPS scans on Ce 3d peaks for Z0.5-Z2 samples.
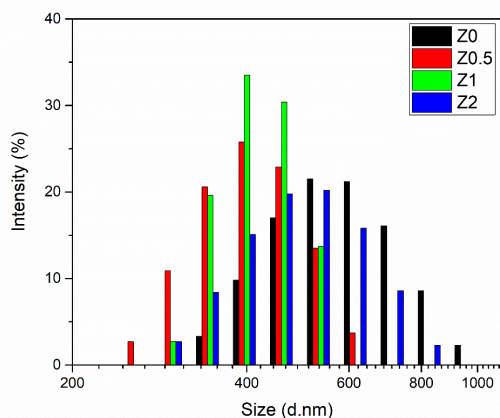
Figure 3. Powder size distribution charts of the samples

3.4 Morphological Analysis

Powder morphologies of the samples are presented in Fig. 4 with their SEM images. Powder morphology is an important parameter that can affect the properties of a material. As seen in Fig. 4, it can be said that ZnO powders produced using the sol-gel method generally have rounded corners and random particle shapes. The SEM images appear consistent with the particle size measurement results. Accordingly, it is seen that the smallest sized particles belong to the Z0.5 sample (Fig. 4 (a)) while the largest sized ZnO powders were observed in the Z0 sample (Fig. 4 (b)). When Figure 5 is examined collectively, it is observed that Ce doping causes a serious decrease in particle size but does not change its morphology. Additionally, it is proved that ZnO samples exhibit a wide particle size distribution in PSD results (Fig. 3), with large and small particles appearing together in SEM images (Fig. 4).

3.5 Photoluminescence Characteristics

The optical characteristics of doped and undoped ZnO powders were investigated using a photoluminescence (PL) experiment at room temperature. The PL emission spectra of ZnO powders with various Ce dopant concentrations are presented in Figure 6. As can be seen from Fig. 5, while all samples are excited around 378 nm, they exhibit emission around 646 nm. This broad green emission peak is typically linked with the existence of band gap defects such as oxygen vacancies, zinc vacancies, and interstitial zinc ion vacancies (Jung *et al*. 2012, Kuo *et al*. 2006, Sinha *et al*. 2014).
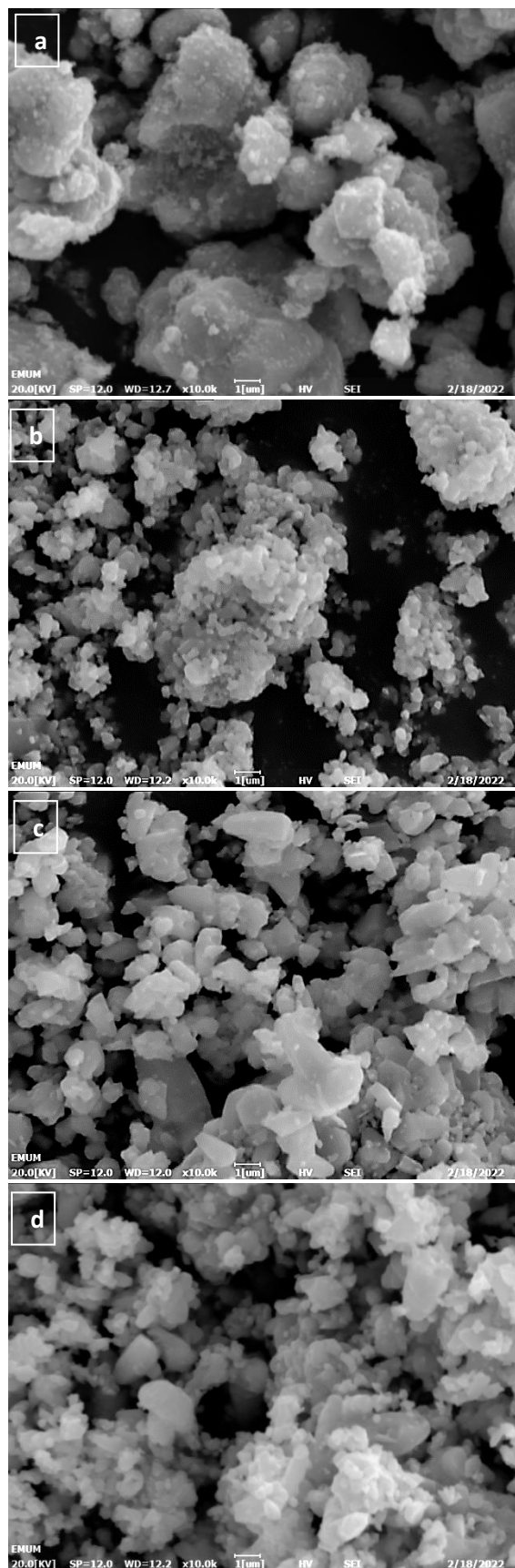

Figure 4. Powder morphologies via SEM images of the (a)Z0, (b)Z0.5, (c)Z1 and (d)Z2 samples

When the effect of doping on PL is examined, it is seen that the emission intensity increases for all Ce dopant ratios. Emission intensity was increased proportionally with 0.5% and 1% doping, while it was decreased with 2% doping ratio (not below the undoped ZnO). The increased intensity of green emission is explained by the additional Ce impurity defects in the ZnO host (Lang *et al*. 2010).
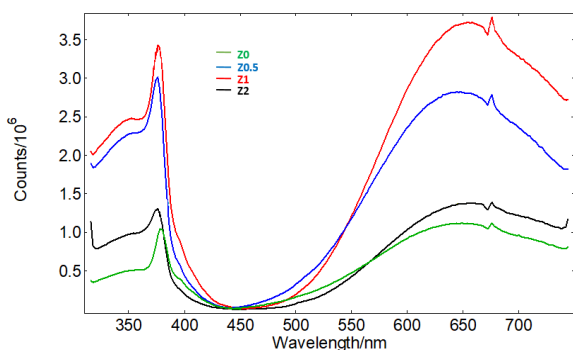

Figure 5. The PL emission spectra of ZnO powders according to the Ce dopant ratios

Depending on the dopant concentration and excitation energy, these newly created defects cause an increase or decrease in the visible area emission intensity (Jayachandraiah and Krishnaiah 2017). Increased dopant ions create numerous electron traps, which inhibit electron-hole pair recombination and reduce emission intensity (W. Li, Wang, Chen, Liao and Li 2017).

3.6 Photocatalytic Results

The maximum absorbance values of methylene blue dye at a wavelength of 664 nm in accordance with time were obtained to observe photocatalytic degradation for each sample. The progression of the degradation mechanism; first, light absorption, followed by stimulated hole and electron separation. Next, photo-generated charge carriers travel toward the catalyst's surface, followed by a redox reaction involving adsorbed reactants (Kar, Smith, and Subramanian 2009).

The time-dependent dissolution curves of MB resolved ZnO-based powders are presented in Fig. 6 (a). Previously, it was stored in the MB solution in the dark, and the deterioration obtained was insignificant. Considering the variation with respect to the initial concentration, it can be seen that the

doped samples exhibit more concentration variation according to Fig. 6(a). Photocatalytic kinetic analyses of the samples were also performed to better understand the kinetics throughout the degradation period. The kinetic mechanism graph given in Fig. 6 (b) is explained by the following formula (2) proposed by Langmuir–Hinshelwood (Kumar *et al*. 2015)
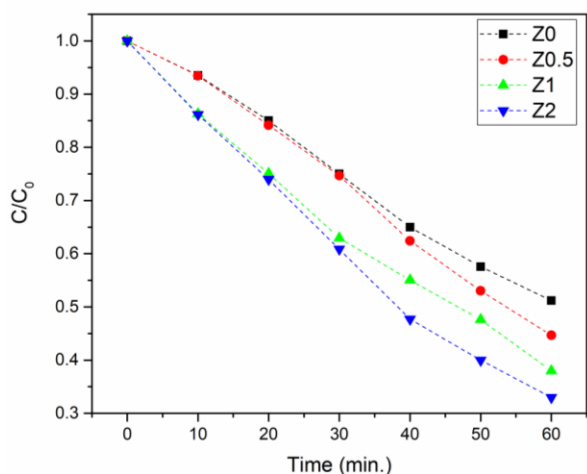
$$\ln\left(\frac{C_o}{C}\right) = kt \qquad (2)$$

where t is the time, C_o corresponds to the original concentration, C represents the comparative concentration and k is the degradation constant. The values of rate constants (k) were found as 0.0120, 0.0136, 0.0147, and 0.0169 min^{-1} for the Z0, Z0.5, Z1, and Z2 samples, respectively. The order of photocatalytic efficiency and photocatalysts k values can be listed as Z2> Z1> Z0.5>Z0.
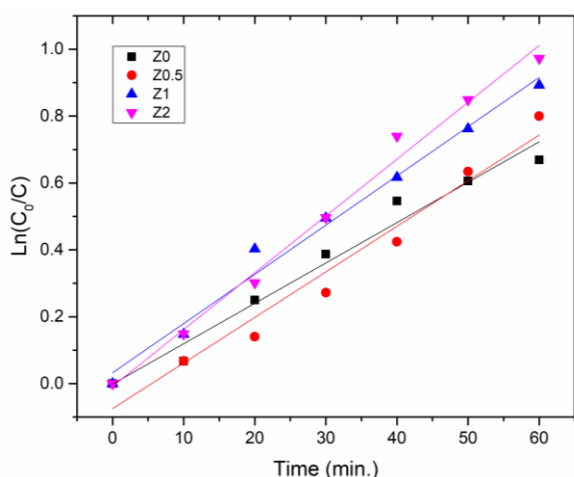
Finally, Fig. 6 (c) shows the photocatalytic degradation efficiencies of the samples. Photocatalytic degradation efficiencies were estimated by the following formula (3);

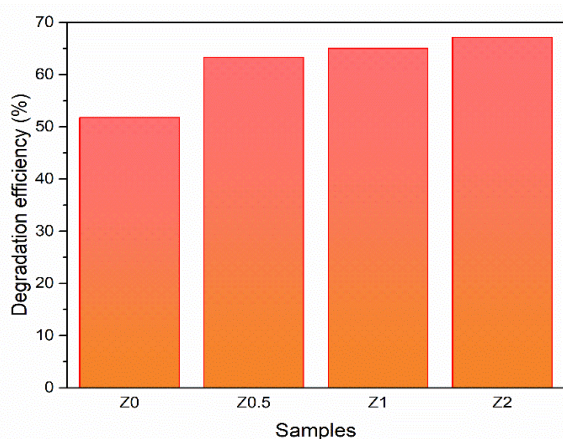$$\eta = \left(\frac{C_o - C}{C_o}\right) \qquad (3)$$

The photocatalytic efficiencies of the Z0, Z0.5, Z1, and Z2 samples after 60 min degradation period was calculated as 51.79%, 63.34%, 65.04 and 67.19, respectively. As can be seen from all of the photocatalytic results in Fig. 7, the photocatalytic properties were affected positively by the doping process. Ce doping in ZnO resulted in significantly improved photocatalytic activity and a significant rise in rate constant values compared to undoped ZnO.

There is no significant morphology, phase, and crystallite size difference between the samples. As can be seen in Fig. 6, the photocatalytic efficiency increased continuously in direct proportion to the dopant ratio. Considering the particle size, which is one of the most important parameters, no correlation was observed between increasing or decreasing particle size and photocatalytic efficiency.

(a)

(b)

(c)

Figure 6. (a) The time-dependent dissolution curves, (b) kinetic constant curves, and (c) the degradation efficiency diagram of the ZnO-based samples

For example, the Z0.5 sample, which has the lowest particle size, does not exhibit the highest photocatalytic efficiency. Since there is not any

regular correlation with other parameters, it can be said that the most effective parameter in terms of photocatalytic efficiency is the dopant ratio.

The increased photocatalytic activity of Ce-doped ZnO photocatalysts is explained by electron and hole migration to the catalytic surface in response to UV irradiation and subsequent involvement in redox reactions with the adsorbed dye (J. Gupta, Barick and Bahadur 2011, Kumar, Kumar and Umar 2014). Ce^{4+} ions can also operate as electron scavengers, trapping conduction band electrons and minimizing or limiting the possibility of electron–hole recombination (Daneshvar, Salari and Khataee 2004). This can efficiently transmit photo-generated electrons to participate in a redox process that produces ·OH free radicals, triggering dye degradation (Djaja and R. 2013). Doping ZnO with Ce^{4+} is predicted to increase surface imperfections and produce trap centers, which form discrete energy levels (impurity states), which lie just below the ZnO conduction band creates the sub-band gap (Anandan and Miyauchi 2011). Because of the trapping-level development, the ZnO band gap narrows, having a significant influence on photocatalytic performance (Choudhary, Bisht, Satpati and Mohapatra 2021). Additionally, Cerium doping improves the visible light usage capability (Choudhary *et al.* 2021). However, with greater Ce concentrations, the number of free electrons reduces due to their entrapment in Ce^{4+} ions, therefore decreases photo-degradation (Kumar *et al*. 2015). Since the doping ratio did not reach the saturation point, no decrease in the photocatalytic efficiency was observed. As the saturation point cannot be reached and the most effective parameter is the dopant ratio, higher Ce dopant ratios may be the subject of future studies.

4. Conclusion

Cerium doped and undoped hexagonal Wurtzite ZnO micro-particles were produced successfully according to the XRD results. Embedding Ce^{4+} ions into the ZnO lattice led to improvement in the crystallite size values of the particles. Ce doping did not cause a change in rounded and random particle morphology but caused changes in particle size

values. The highest particle size belongs to the undoped ZnO particle, while the 0.5% Ce-doped ZnO sample has the lowest particles in size. Additionally, Ce doping process provided improvement in the optical properties, including photoluminescence and photocatalysis by increasing the emission intensities and photocatalytic rate constant values. It was determined that the most effective parameter in terms of photocatalytic efficiency is the Ce dopant ratio as there is not any correlation with other parameters.

5. References

Al Abdullah, K., Awad, S., Zaraket, J., & Salame, C., 2017. Synthesis of ZnO nanopowders by using sol-gel and studying their structural and electrical properties at different temperature. *Energy Procedia,* **119**, 565-570.

Anandan, S., & Miyauchi, M., 2011. Ce-doped ZnO (CexZn1-xO) becomes an efficient visible-light-sensitive photocatalyst by co-catalyst (Cu^{2+}) grafting. *Physical Chemistry Chemical Physics,* **13(33)**, 14937-14945.

Bomila, R., Suresh, S., & Srinivasan, S., 2019. Synthesis, characterization and comparative studies of dual doped ZnO nanoparticles for photocatalytic applications. *Journal of Materials Science-Materials in Electronics, 30***(1)**, 582-592.

Chelouche, A., Touam, T., Tazerout, M., Boudjouan, E., Djouadi, D., & Doghmane, A., 2017. Low cerium doping investigation on structural and photoluminescence properties of sol-gel ZnO thin films. *Journal of Luminescence,* **181**, 448-454.

Choudhary, S., Bisht, A., Satpati, B., & Mohapatra, S. 2021. Facile synthesis of Ce-doped ZnO nanospindles for photocatalytic applications. *Applied Physics a-Materials Science & Processing,* **127(12)**, 1-14.

Daneshvar, N., Salari, D., & Khataee, A. R., 2004. Photocatalytic degradation of azo dye acid red 14 in water on ZnO as an alternative catalyst to TiO₂. Journal of Photochemistry and Photobiology a-Chemistry, 162**(2-3)**, 317-322.

Djaja, N. F., & R., S., 2013. Characteristics and Photocatalytics Activities of Ce-Doped ZnO Nanoparticles. Materials Sciences and Applications, **4(2)**, 145-152.

Demirci, S., Dikici, T., Tuncay, M. M., & Kaya, N., 2020. A study of heating rate effect on the photocatalytic performances of ZnO powders prepared by sol-gel route: Their kinetic and thermodynamic studies. *Applied Surface Science,* **507,** 145083.

Gupta, A., Saurav, J. R., & Bhattacharya, S., 2015. Solar light based degradation of organic pollutants using ZnO nanobrushes for water filtration. *Rsc Advances,* **5(87)**, 71472-71481.

Gupta, J., Barick, K. C., & Bahadur, D. 2011. Defect mediated photocatalytic activity in shape-controlled ZnO nanostructures. *Journal of Alloys and Compounds,* **509(23)**, 6725-6730.

Jayachandraiah, C., & Krishnaiah, G., 2017. Influence of cerium dopant on magnetic and dielectric properties of ZnO nanoparticles. *Journal of Materials Science,* **52(12)**, 7058-7066.

Jung, Y. I., Noh, B. Y., Lee, Y. S., Baek, S. H., Kim, J. H., & Park, I. K., 2012. Visible emission from Ce-doped ZnO nanorods grown by hydrothermal method without a post thermal annealing process. *Nanoscale Research Letters, 7(1)*, 1-5 .

Kar, A., Smith, Y. R., & Subramanian, V., 2009. Improved Photocatalytic Degradation of Textile Dye Using Titanium Dioxide Nanotubes Formed Over Titanium Wires. *Environmental Science & Technology,* **43(9)**, 3260-3265.

Karidas, S., Veena, B. K., Pujari, N., Krishna, P., & Chunduru, V., 2020. Photodegradation of Methylene Blue (MB) using Cerium-doped Zinc Oxide nanoparticles. *Sadhana-Academy Proceedings in Engineering Sciences,* **45(1),** 1-9.

Keskin, O. Y., Dalmis, R., Birlik, I., & Azem, N. F. A. 2020. Comparison of the effect of non-metal and rare-earth element doping on structural and optical properties of CuO/TiO₂ one-dimensional photonic crystals. *Journal of Alloys and Compounds,* **817***, 153262*.

Kumar, R., Kumar, G., & Umar, A., 2014. Zinc Oxide Nanomaterials for Photocatalytic Degradation of Methyl Orange: A Review. *Nanoscience and Nanotechnology Letters,* **6(8)**, 631-650.

Kumar, R., Umar, A., Kumar, G., Akhtar, M. S., Wang, Y., & Kim, S. H., 2015. Ce-doped ZnO nanoparticles for efficient photocatalytic degradation of direct red-23 dye. *Ceramics International,* **41(6)**, 7773-7782.

Kuo, S. Y., Chen, W. C., Lai, F. I., Cheng, C. P., Kuo, H. C., Wang, S. C., & Hsieh, W. F., 2006. Effects of doping concentration and annealing temperature on properties of highly-oriented al-doped ZnO films. *Journal of Crystal Growth,* **287(1**), 78-84.

Lang, J. H., Han, Q., Yang, J. H., Li, C. S., Li, X., Yang, L. L., Cao, J., 2010. Fabrication and optical properties of Ce-doped ZnO nanorods. *Journal of Applied Physics,* **107(7)**, 074302.

Li, H. L., Lv, Y. B., Li, J. Z., & Yu, K., 2014. Experimental and first-principles studies of structural and optical properties of rare earth (RE = La, Er, Nd) doped ZnO. *Journal of Alloys and Compounds,* **617**, 102-107.

Li, L., Liu, Z. Y., Zhang, Q. Q., Meng, C. H., Zhang, T. R., & Zhai, J., 2015. Underwater superoleophobic porous membrane based on hierarchical TiO_2 nanotubes: multifunctional integration of oil-water separation, flow-through photocatalysis and self-cleaning. *Journal of Materials Chemistry A,* **3(3)**, 1279-1286.

Li, W., Wang, G. J., Chen, C. E. H., Liao, J. C., & Li, Z. C., 2017. Enhanced Visible Light Photocatalytic Activity of ZnO Nanowires Doped with Mn^{2+} and Co^{2+} Ions. *Nanomaterials,* **7(1)**, 20.

Pathak, T. K., Coetsee-Hugo, E., Swart, H. C., Swart, C. W., & Kroon, R. E., 2020. Preparation and characterization of Ce doped ZnO nanomaterial for photocatalytic and biological applications. *Materials Science and Engineering B-Advanced Functional Solid-State Materials,* **261**, *114780*.

Reddy, I. N., Reddy, C. V., Sreedhar, M., Shim, J., Cho, M., & Kim, D., 2019. Effect of ball milling on optical properties and visible photocatalytic activity of Fe doped ZnO nanoparticles. *Materials Science and Engineering B-Advanced Functional Solid-State Materials,* **240**, 33-40.

Savolainen, K., Pylkkanen, L., Norppa, H., Falck, G., Lindberg, H., Tuomi, T., Seipenbusch, M. 2010. Nanotechnologies, engineered nanomaterials and occupational health and safety - A review. *Safety Science,* **48(8)**, 957-963.

Sharma, D. K., Sharma, K. K., Kumar, V., & Sharma, A., 2016. Effect of Ce doping on the structural, optical and magnetic properties of ZnO nanoparticles. *Journal of Materials Science-Materials in Electronics,* **27(10)**, 10330-10335.

Sin, J. C., Lam, S. M., Lee, K. T., & Mohamed, A. R. 2014. Preparation of rare earth-doped ZnO hierarchical micro/nanospheres and their enhanced photocatalytic activity under visible light irradiation. *Ceramics International,* **40(4)**, 5431-5440.

Singh, P., & Borthakur, A. 2018. A review on biodegradation and photocatalytic degradation of organic pollutants: A bibliometric and comparative analysis. *Journal of Cleaner Production,* **196**, 1669-1680.

Sinha, N., Ray, G., Bhandari, S., Godara, S., & Kumar, B., 2014. Synthesis and enhanced properties of cerium doped ZnO nanorods. *Ceramics International,* **40(8)**, 12337-12342.

Subramanian, M., Thakur, P., Tanemura, M., Hihara, T., Ganesan, V., Soga, T., Jimbo, T. 2010. Intrinsic ferromagnetism and magnetic anisotropy in Gd-doped ZnO thin films synthesized by pulsed spray pyrolysis method. *Journal of Applied Physics,* **108(5)**, 053904.

Thambidurai, M., Muthukumarasamy, N., Velauthapillai, D., & Lee, C., 2014. Rosa centifolia sensitized ZnO nanorods for photoelectrochemical solar cell applications. *Solar Energy,* **106**, 143-150.

Xu, C. P., Anusuyadevi, P. R., Aymonier, C., Luque, R., & Marre, S., 2019. Nanostructured materials for photocatalysis. *Chemical Society Reviews,* **48(14)**, 3868-3902.

Yang, L., Gao, M. G., Dai, B., Guo, X. H., Liu, Z. Y., & Peng, B. H., 2016. Synthesis of spindle-shaped AgI/TiO_2 nanoparticles with enhanced photocatalytic performance. *Applied Surface Science,* **386**, 337-344.

Zamiri, R., Lemos, A. F., Reblo, A., Ahangar, H. A., & Ferreira, J. M. F., 2014. Effects of rare-earth (Er, La and Yb) doping on morphology and structure properties of ZnO nanostructures prepared by wet chemical method. *Ceramics International,* **40(1)**, 523-529.